

A modified atmospheric non-hydrostatic model on low aspect ratio grids: part II

By WEN-YIH SUN^{1,2,3*}, OLIVER M. SUN⁴ and KAZUHISA TSUBOKI³,

¹*Department of Earth, Atmospheric and Planetary Sciences, Purdue University, West Lafayette, IN 47907, USA;*

²*Department of Atmospheric Sciences, National Central University, Chung-Li, Tao-yuan, 320, Taiwan;*

³*Hydrospheric Atmospheric Research Center (HyARC), Nagoya University, Nagoya, 464-8601, Japan;*

⁴*Department of Physical Oceanography, Woods Hole Oceanographic Institute, Woods Hole, MA 02543, USA*

(Manuscript received 6 September 2012; in final form 24 May 2013)

ABSTRACT

Sun et al. (2012) proposed a modified non-hydrostatic model (MNH), in which the left-hand side of the continuity equation is multiplied by a parameter δ ($4 \leq \delta \leq 16$ in the article) to suppress high-frequency acoustic waves. They showed that the MNH allows a longer time step than the original non-hydrostatic model (NH). The MNH is also more accurate and efficient than the horizontal explicit and vertical implicit scheme (HE–VI) when the aspect ratio ($\Delta x/\Delta z$) is small. In addition to multiplying a parameter δ , here we propose to add a smoothing on the right-hand side of the continuity equation in the MNH to damp shortest sound waves. Linear stability analysis and non-linear model simulations show that the MNH with smoothing (henceforth abbreviated as MNHS) can use twice the time interval of the MNH while maintaining the same accuracy. The MNHS is also more accurate and efficient than HE–VI when the aspect ratio is small.

Keywords: non-hydrostatic model, eigenvalue, forward–backward, aspect ratio, gravity wave, HE–VI

1. Introduction

The eigenvalues and non-linear simulations of the non-hydrostatic model (NH) using the conventional forward–backward scheme (FB) (Mesinger and Arakawa, 1976; Sun, 1980, 1984), the horizontal explicit and vertical implicit scheme (HE–VI) (Klemp and Wilhelmson, 1978; Saito, 2007) and the modified non-hydrostatic model (MNH) have been discussed in Sun et al. (2012), hereafter referred to as Part I. The MNH is designed to suppress high-frequency acoustic waves by multiplying the left-hand side of the continuity equation by a parameter δ , where $16 \geq \delta \geq 4$. When $\delta = 1$, the MNH and NH are identical. Since the FB is applied to solve NH and MNH, they called their approach a modified forward–backward scheme (MFB) for $\delta > 1$; MFB is the same as the conventional FB when $\delta = 1$.

In Part I, frequency of acoustic waves is greatly reduced by the MFB, but much less so for gravity waves. Also, the MFB is more accurate for smaller values of δ or finer space

intervals. The non-linear non-hydrostatic Cloud Resolving Storm Simulator (CReSS; Tsuboki and Sakakibara, 2002, 2007) showed that Kelvin–Helmholtz instabilities, thermal bubbles and mountain waves simulated by a conventional FB can be reproduced using an MFB with a time interval four times longer. It was also found that the shortest waves (i.e. $2\Delta x$ and/or $2\Delta z$) require the shortest time interval according to the Courant–Friedrich–Lewy (CFL) criterion. Since the accuracy of gravity waves decreases as δ increases, it seems preferable to filter $2\Delta x$ and $2\Delta z$ waves rather than increase the value of δ . Hence, in addition to multiplying δ ($\delta \leq 16$ in Part I) in the continuity equation of MNH, we propose to apply smoothing on the right hand of the continuity equation to damp the short waves. We refer to the resulting model as the modified non-hydrostatic model with smoothing (MNHS). The eigenvalue and non-linear model simulations show that, for the same accuracy, MNHS allows twice the time interval of MNH. It is also noted that other numerical schemes, for example: the modified leapfrog scheme (Sun and Sun, 2011) and/or the new semi-implicit scheme (Sun, 2011) can be applied to the wave-related terms of the MNHS to achieve the same efficiency as discussed in this paper.

*Corresponding author.
email: wysun@purdue.edu

2. Basic and linearised equations

The 2-D non-hydrostatic equations for the dry atmosphere can be written as:

$$\frac{\partial u}{\partial t} + u \frac{\partial u}{\partial x} + w \frac{\partial u}{\partial z} = -\frac{1}{\rho} \frac{\partial p}{\partial x} + D_u \quad (1)$$

$$\frac{\partial w}{\partial t} + u \frac{\partial w}{\partial x} + w \frac{\partial w}{\partial z} = -\frac{1}{\rho} \frac{\partial p}{\partial z} - g + D_w \quad (2)$$

$$\frac{\partial \theta}{\partial t} + u \frac{\partial \theta}{\partial x} + w \frac{\partial \theta}{\partial z} = D_\theta \quad (3)$$

$$\frac{\partial \rho}{\partial t} = -\left(\frac{\partial \rho u}{\partial x} + \frac{\partial \rho w}{\partial z}\right) \quad (4)$$

$$p = \rho R T \quad (5)$$

$$\theta = T \left(\frac{P_0}{P} \right)^{R/C_p} \quad (6)$$

where u and w are the x and z components of wind; p is pressure; θ is potential temperature; T is temperature; ρ is density; R is gas constant; C_p is specific heat at constant pressure; D_u and D_w are momentum diffusions along the x and z directions; D_θ is the heat diffusion. The linearised equations become:

$$\frac{\partial u'}{\partial t} + \frac{1}{\rho_0} \frac{\partial p'}{\partial x} = 0 \quad (7)$$

$$\frac{\partial w'}{\partial t} + \frac{1}{\rho_0} \frac{\partial p'}{\partial z} + g \frac{\rho'}{\rho_0} = 0 \quad (8)$$

$$\frac{\partial \theta'}{\partial t} + w' \frac{\partial \theta_0}{\partial z} = 0 \quad (9)$$

$$\frac{\partial \rho'}{\partial t} + \rho_0 \left(\frac{\partial u'}{\partial x} + \frac{\partial w'}{\partial z} \right) + w' \frac{\partial \rho_0}{\partial z} = 0 \quad (10)$$

$$\rho' = \frac{p'}{C^2} - \frac{\rho_0 \theta'}{\theta_0} \quad (11)$$

where primes indicate deviations from the basic state variables (with subscript '0'), which are functions of height only, and $C = \sqrt{(c_p/c_v) R T_0}$. The basic state wind is assumed to be zero. In Part I, $\delta > 1$ was introduced in the continuity equation in order to filter high-frequency acoustic waves. Following the procedure in Part I, eqs. (7)–(11) can be formulated as:

$$\frac{\partial \hat{u}}{\partial t} + \frac{\partial \hat{p}}{\partial x} = 0 \quad (12)$$

$$\frac{\partial \hat{w}}{\partial t} + \frac{\partial \hat{p}}{\partial z} + \left(\frac{g}{C^2} + \frac{R_0}{2} \right) \hat{p} - g \hat{\theta} = 0 \quad (13)$$

$$\frac{\partial \hat{\theta}}{\partial t} + \hat{w} S_0 = 0 \quad (14)$$

$$\frac{\partial \hat{p}}{\partial t} = -\frac{C^2}{\delta} \left(\frac{\partial \hat{u}}{\partial x} + \frac{\partial \hat{w}}{\partial z} + \left(S_0 + \frac{R_0}{2} \right) \hat{w} \right) \quad (15)$$

where $\hat{p} = p'/\sqrt{\rho_0}$, $\hat{\theta} = \sqrt{\rho_0} \theta'/\theta_0$, $\hat{u} = u'\sqrt{\rho_0}$, $\hat{w} = w'\sqrt{\rho_0}$, $S_0 = \frac{\partial \theta_0}{\partial_0 \partial z}$, and $R_0 = \frac{\partial \rho_0}{\partial_0 \partial z}$.

The linearised equations show that the $2\Delta x$ and/or $2\Delta z$ waves require the shortest Δt to satisfy the CFL criterion. Therefore, to relax the time step limitation, we apply smoothing on the right-hand side of eq. (15). Thus, eq. (15) is replaced by

$$\frac{\partial \hat{p}}{\partial t} = \frac{C^2}{\delta} \bar{f}^{xz} \quad (16)$$

where

$$f = -\left[\frac{\partial \hat{u}}{\partial x} + \frac{\partial \hat{w}}{\partial z} + \left(S_0 + \frac{R_0}{2} \right) \hat{w} \right]$$

and

$$\begin{aligned} \bar{f}^{xz} &= (\bar{f}^x)^z = \left(\frac{f_{p-1,q} + 2f_{p,q} + f_{p+1,q}}{4} \right)^z \\ &= \cos^2\left(\frac{k\Delta x}{2}\right) \cos^2\left(\frac{m\Delta z}{2}\right) f \end{aligned}$$

is the two-dimensionally smoothed version of f . Where k and m are the wave numbers in the x and z directions, respectively. Equation (15) can now be written

$$\begin{aligned} \frac{\partial \hat{p}}{\partial t} &= \frac{C^2}{\delta} \bar{f}^{xz} = -\frac{C^2 \cos^2\left(\frac{k\Delta x}{2}\right) \cos^2\left(\frac{m\Delta z}{2}\right)}{\delta} \\ &\times \left(\frac{\partial \hat{u}}{\partial x} + \frac{\partial \hat{w}}{\partial z} + \left(S_0 + \frac{R_0}{2} \right) \hat{w} \right) \\ &= -\frac{C^2}{\tilde{\delta}} \left(\frac{\partial \hat{u}}{\partial x} + \frac{\partial \hat{w}}{\partial z} + \left(S_0 + \frac{R_0}{2} \right) \hat{w} \right) \end{aligned} \quad (17)$$

and

$$\tilde{\delta} \equiv \frac{\delta}{\cos^2\left(\frac{k\Delta x}{2}\right) \cos^2\left(\frac{m\Delta z}{2}\right)} \quad (18)$$

Equations (17) and (18) indicate that $2\Delta x$ and $2\Delta z$ waves are removed from convergence/divergence. The $3\Delta x$ and $3\Delta z$ waves, which can create non-linear instability, are also significantly reduced by the second-order smoothing. The effect of smoothing decreases with increasing wavelength. The value of $\cos(k\Delta x/2) = 0.809$ for a $5\Delta x$ -wave seems to imply that the errors can be quite large for $5\Delta x$ and shorter waves according to eq. (17). However, linear stability analysis shows that smoothing does not significantly affect the results for wavelengths longer than $3\Delta x$. Non-linear model simulations also reveal that the accuracy of the MNH (without smoothing) is comparable to that of the MNHS (with smooth) for the same value of δ , even when the time interval for MNHS is twice that for MNH. In Section 3, we will show the eigenvalues of the MNH, MNHS and HE-VI models, as well as their comparisons with , the eigenvalue of

gravity waves derived from the differential in time and difference in space [eq. (2. 18) in Part I]:

$$\sigma_g^2 = \left\{ \left[C^2 \left(X^2 + Z^2 + \Gamma_0^2 + \frac{gS_0}{C^2} \right) \right] - \sqrt{\left[C^2 \left(X^2 + Z^2 + \Gamma_0^2 + \frac{gS_0}{C^2} \right) \right]^2 - 4C^2 gS_0 X^2} \right\} / 2 \quad (19)$$

where $\Gamma_0 = -\frac{g}{C^2} - \frac{R_0}{2} = S_0 + \frac{R_0}{2}$; $X = \frac{\sin(k\Delta x/2)}{\Delta x/2}$; and $Z = \frac{\sin(m\Delta z/2)}{\Delta z/2}$.

3. Eigenvalue of finite difference equations

The solutions of eqs. (12)–(15) can be assumed:

$$\begin{bmatrix} \hat{\theta} \\ \hat{p} \\ \hat{u} \\ \hat{w} \end{bmatrix} (p\Delta x, q\Delta z, n\Delta t) = \tilde{\lambda}^n \begin{bmatrix} \Theta \\ P \\ U \\ W \end{bmatrix} e^{i(kp\Delta x + mq\Delta z)} \quad (20)$$

where $\tilde{\lambda}$ is the complex amplification factor.

3.1. The finite difference form and eigenvalues of the modified FB

Following Part I, the Arakawa C grids are used in the eigenvalue analysis; a forward in time scheme is applied to the momentum fields and a backward to the pressure and temperature, producing finite difference equations for eqs. (12)–(15),

$$\left(\frac{\tilde{\lambda} - 1}{\Delta t} \right) U + iXP = 0 \quad (21)$$

$$\left(\frac{\tilde{\lambda} - 1}{\Delta t} \right) W + (iZ - \Gamma_0)P - g\Theta = 0 \quad (22)$$

$$\left(\frac{\tilde{\lambda} - 1}{\Delta t} \right) \frac{\tilde{\delta}P}{C^2} + i\tilde{\lambda}XU + \tilde{\lambda}(iZ + \Gamma_0)W = 0 \quad (23)$$

$$\left(\frac{\tilde{\lambda} - 1}{\Delta t} \right) \Theta + \tilde{\lambda}S_0W = 0 \quad (24)$$

The eigenvalues for the modified forward-backward scheme with smoothing (MFBS) can now be determined from

$$\frac{\tilde{\delta}}{C^2} \left(\frac{\tilde{\lambda} - 1}{\Delta t} \right)^4 + \left(\frac{\tilde{\lambda} - 1}{\Delta t} \right)^2 \tilde{\lambda} \left[X^2 + Z^2 + \Gamma_0^2 + \frac{\tilde{\delta}gS_0}{C^2} \right] + \tilde{\lambda}^2 gS_0 X^2 = 0 \quad (25)$$

or

$$\frac{\delta}{C^2 \cos^2(\frac{k\Delta x}{2}) \cos^2(\frac{m\Delta z}{2})} \left(\frac{\tilde{\lambda} - 1}{\Delta t} \right)^4 + \left(\frac{\tilde{\lambda} - 1}{\Delta t} \right)^2 \tilde{\lambda} \left[X^2 + Z^2 + \Gamma_0^2 + \frac{\delta gS_0}{C^2 \cos^2(\frac{k\Delta x}{2}) \cos^2(\frac{m\Delta z}{2})} \right] + \tilde{\lambda}^2 gS_0 X^2 = 0 \quad (26)$$

Without smoothing, eqs. (25) and (26) are identical to eq. (3.6) of Part I, which consists of two acoustic waves and two gravity waves. Let us define:

$$\Delta \tilde{t}_\delta = 2 \sqrt{\tilde{\delta} / \left[C^2 \left(X^2 + Z^2 + \Gamma_0^2 + \frac{\tilde{\delta}gS_0}{C^2} \right) \right]} \quad (27)$$

The amplification $|\tilde{\lambda}|$ factor is then unity if $\Delta t \leq \Delta \tilde{t}_\delta$. In that case, the frequency $\tilde{\omega}_\delta$ is defined by

$$\tilde{\lambda} = \tilde{\lambda}_r + i\tilde{\lambda}_i = |\tilde{\lambda}| \exp(-i\tilde{\omega}_\delta \Delta t) = \cos(\tilde{\omega}_\delta \Delta t) - i \sin(\tilde{\omega}_\delta \Delta t) \quad (28)$$

and

$$\tilde{\omega}_\delta = -\tan^{-1}(\tilde{\lambda}_i/\tilde{\lambda}_r)/\Delta t \quad (29)$$

Without smoothing, the values of $\tilde{\lambda}$, $\tilde{\omega}_\delta$, and $\Delta \tilde{t}_\delta$ of eqs. (25)–(29) are also equal to λ_δ , ω_δ , and Δt_δ of MFB discussed in Part I.

With $g = 10 \text{ m s}^{-2}$, $C = 300 \text{ m s}^{-1}$, $\Delta x = 400 \text{ m}$, $\Delta z = 125 \text{ m}$, $S_0 = 1.0 \times 1.0^{-5} \text{ m}^{-1}$ and $\delta = 16$, we obtain $\Delta t_{\delta=16} = 1.59 \text{ s}$ according to eq. (27) without smoothing. Figure 1 shows that: (a) the frequency of $\omega_{\delta=16}$ (from 0.002 near the right-bottom corner to 0.009 s^{-1} with interval of 0.001 s^{-1}) and $\omega_{\delta=16} - \sigma_g$ (from -3.5×10^{-6} to $-5.0 \times 10^{-7} \text{ s}^{-1}$); (b) $\tilde{\omega}_{\delta=4}$ and $\tilde{\omega}_{\delta=4} - \sigma_g$ (from -8×10^{-7} to $-1.0 \times 10^{-7} \text{ s}^{-1}$); and (c) $\tilde{\omega}_{\delta=16}$ and $\tilde{\omega}_{\delta=16} - \sigma_g$ (from $-4. \times 10^{-6}$ to $-5.0 \times 10^{-7} \text{ s}^{-1}$). Smoothing of the continuity equation creates a large error for the $2\Delta x$ (and/or $2\Delta z$) waves in Fig. 1b and c. Because those short-waves cannot be calculated accurately using the finite difference schemes, the eigenvalues of the unwanted $2\Delta x$ and $2\Delta z$ waves are not presented here. The error associated with smoothing decreases drastically with increasing wavelength. The errors for $3\Delta x$ waves, of $-8 \times 10^{-7} \text{ s}^{-1}$ in Fig. 1b and $-3.5 \times 10^{-6} \text{ s}^{-1}$ in Fig. 1c, are comparable with the errors at longer wavelengths. With approximately the same Δt ($\sim 1.6 \text{ s}$), the maximum value of $\tilde{\omega}_{\delta=4} - \sigma_g$ ($= |8 \times 10^{-7}| \text{ s}^{-1}$) is much less than the maximum of $\omega_{\delta=16} - \sigma_g$ ($= |3.5 \times 10^{-6}| \text{ s}^{-1}$). The error of $\tilde{\omega}_{\delta=16}$ ($= |4 \times 10^{-6}| \text{ s}^{-1}$) is also comparable with the error of $\omega_{\delta=16}$ ($= |3.5 \times 10^{-6}| \text{ s}^{-1}$), where the time interval used for $\tilde{\omega}_{\delta=16}$ ($\Delta t = 3.08 \text{ s}$) is twice that for $\omega_{\delta=16}$ ($\Delta t = 1.59 \text{ s}$).

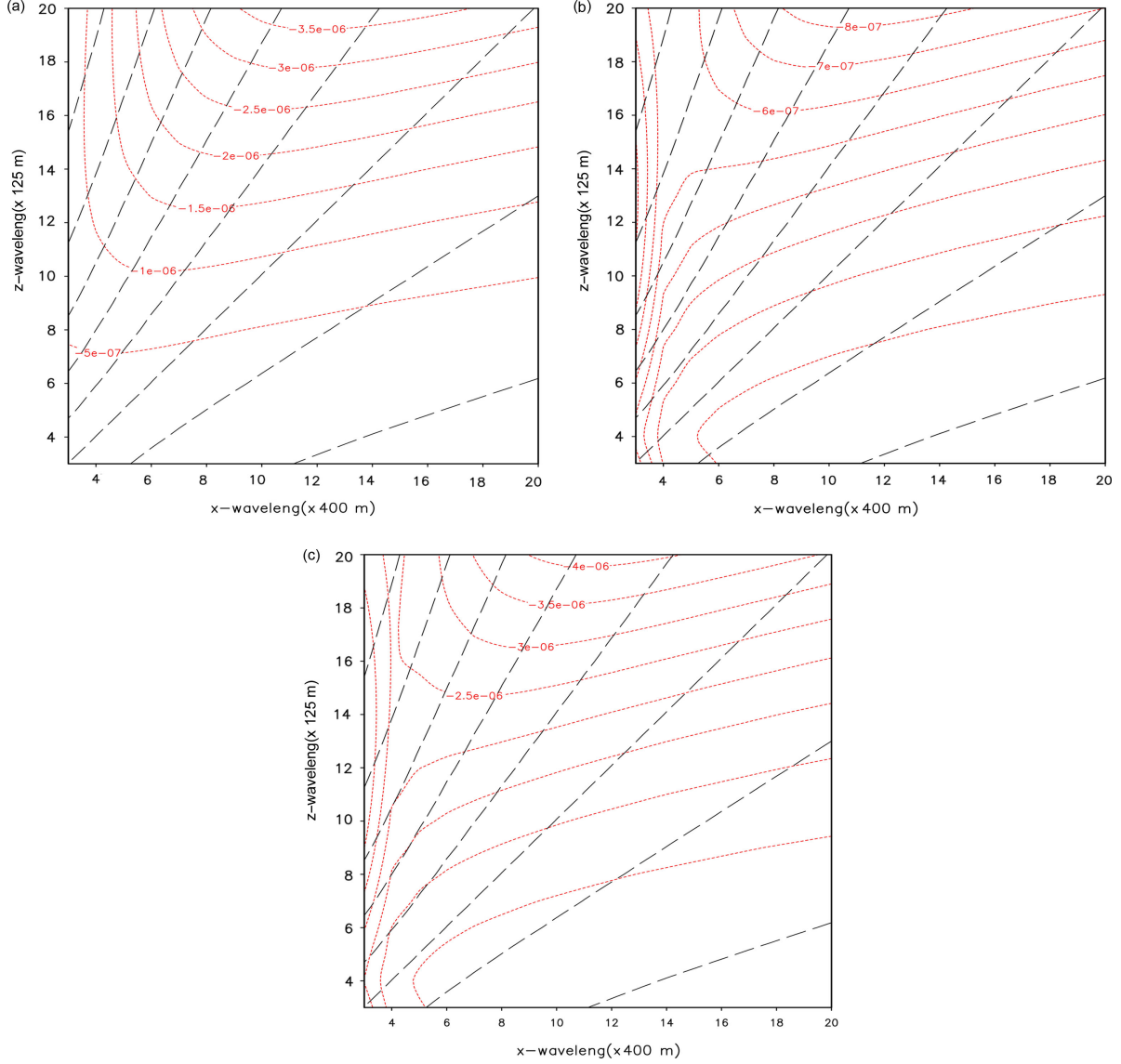


Fig. 1. Frequency of gravity wave with $g = 10 \text{ m s}^{-2}$, $C = 300 \text{ m s}^{-1}$, $\Delta x = 400 \text{ m}$, $\Delta z = 125 \text{ m}$, and $S_o = 1.0 \times 10^{-5} \text{ m}^{-1}$: (a) $\omega_{\delta=16}$ ($\Delta t = 1.59 \text{ s}$, dash) and $\omega_{\delta=16} - \sigma_g$ (dot); (b) $\tilde{\omega}_{\delta=4}$ ($\Delta t = 1.68 \text{ s}$) and $\tilde{\omega}_{\delta=4} - \sigma_g$; and (c) $\tilde{\omega}_{\delta=16}$ ($\Delta t = 3.18 \text{ s}$) and $\tilde{\omega}_{\delta=16} - \sigma_g$.

When the basic state remains the same and $\Delta x = 5 \text{ m}$ and $\Delta z = 5 \text{ m}$, $\Delta t_{\delta=16} = 4.71 \times 10^{-2} \text{ s}$ according to eq. (27) without smoothing. Figure 2a shows that the frequency of $\omega_{\delta=16}$ ($\Delta t = 4.71 \times 10^{-2} \text{ s}$) is from 0.002 to 0.009 s^{-1} , and $\omega_{\delta=16} - \sigma_g$ is from -2.5×10^{-8} to $2.0 \times 10^{-8} \text{ s}^{-1}$. With smoothing, $\delta = 16$, and $\Delta t = 9.42 \times 10^{-2} \text{ s}$, $\tilde{\omega}_{\delta=16}$ and $\tilde{\omega}_{\delta=16} - \sigma_g$ (from -3.5×10^{-9} to $5.0 \times 10^{-10} \text{ s}^{-1}$) are shown in Fig. 2b. The accuracy of $\tilde{\omega}_{\delta=16}$ is better than $\omega_{\delta=16}$, which indicates that smoothing of the continuity equation does not deteriorate the accuracy of eigenvalues in the fine resolution case. Part I showed that the MNH (with $\delta = 16$) is capable of reproducing the FB results with a time interval four times longer. When spatial smoothing

is added to MNH, the allowable time interval becomes eight times that of FB, according to linearised equations, without significantly reducing the accuracy. Note also that Part I showed that in a fine-resolution model with small aspect ratio, the MFB is more accurate and efficient than HE-VI.

4. Numerical simulations

The non-linear non-hydrostatic CReSS (Tsuboki and Sakakibara, 2002, 2007), has been applied to simulate shear instability, thermal bubbles, and mountain waves with the FB, MFB, MFBS and HE-VI. CReSS uses

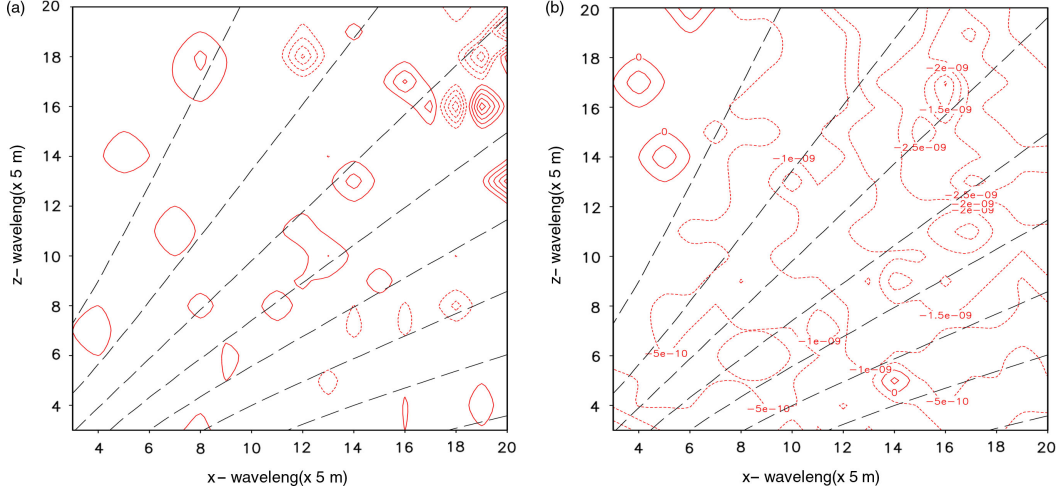


Fig. 2. (a) Frequency of $\omega_{\delta=16}$ ($\Delta t = 4.71 \times 10^{-2}$ s, dash) from 0.002 (dashed line at right-bottom corner) to 0.009 s^{-1} with interval of $.001 \text{ s}^{-1}$, and $\omega_{\delta=16} - \sigma_g$ (dot) from -2.5×10^{-8} to $2.0 \times 10^{-8} \text{ s}^{-1}$ with interval of $1.0 \times 10^{-9} \text{ s}^{-1}$; (b) $\omega_{\delta=16}$ ($\Delta t = 9.42 \times 10^{-2}$ s and smoothing), and $\omega_{\delta=16} - \sigma_g$ from -3.5×10^{-9} to $5.0 \times 10^{-10} \text{ s}^{-1}$ with interval of $5.0 \times 10^{-10} \text{ s}^{-1}$.

Arakawa C and Lorenz staggered grids in the horizontal and vertical, respectively. Prognostic variables consist of the 3-D velocity components, perturbations of pressure and potential temperature, water vapour mixing ratio, subgrid scale turbulent kinetic energy (TKE) and cloud physical variables. In the FB version of CReSS, u , v and w are calculated using forward-differences, while the pressure perturbation p' uses the backward-difference with a small time interval (Δt_s). The non-linear and other forcing terms, which are calculated at a larger time interval ($\Delta t_b = n\Delta t_s$), remain constant when integrating sound waves. The leapfrog scheme is applied to the advection terms. The model also includes viscosity and divergence damping of the pressure gradient force in the momentum equations. In the HE-VI, the forward difference is applied to calculate

u and v . Then, the implicit scheme is applied to solve w and p' using a tri-diagonal matrix solver, as discussed in Saito (2007). The detailed equations and numerical schemes are referred to Tsuboki and Sakakibara (2007). There is no analytical solution to the non-linear eqs. (1)–(6). Hence, the results of the conventional FB ($\delta = 1$) will be used as the references to compare with the simulations from the HE-VI, MFB and the new MFBS.

4.1. Large Kelvin-Helmholtz wave with $\Delta x = 10 \text{ m}$ and $\Delta z = 5 \text{ m}$

The initial x-component wind u is shown in Fig. 3a. The initial background potential temperature and elliptic-type perturbation with the amplitude of -0.4 K , and the

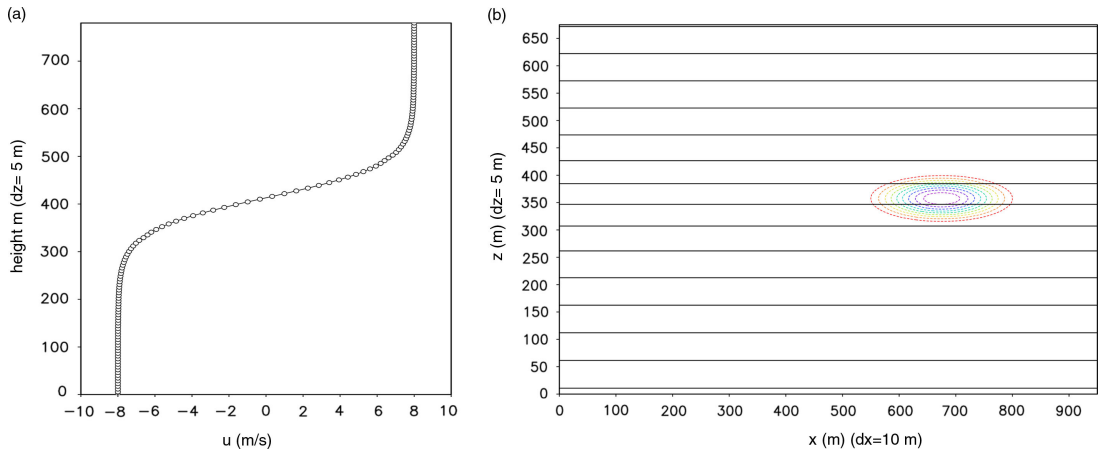


Fig. 3. (a) Initial x-component wind for Kelvin-Helmholtz instability for Section 4.1–4.2; (b) initial background θ_0 (solid) and perturbation θ' (dot) for large-scale waves discussed in Section 4.1.

horizontal and vertical radii of 180 m and 60 m are shown in Fig. 3b. Figure 4a shows the simulated potential temperatures θ at $t = 320$ s with $\Delta t_b = 0.4$ s from: FB with $\Delta t_s = 0.01$ s; MFB with $\delta = 16$, $\Delta t_s = 0.04$ s; MFBS with $\delta = 4$, $\Delta t_s = 0.04$ s; MFBS with $\delta = 16$, $\Delta t_s = 0.08$ s; and HE-VI with $\Delta t_s = 0.02$ s. The five simulations nearly coincide. The differences between $\theta_{\text{MFBS}}(\delta = 4, \Delta t_s = 0.04$ s) and $\theta_{\text{FB}}(\delta = 1, \Delta t_s = 0.01$ s) range from -0.03 to 0.03 K, (Fig. 4b). Meanwhile, $\theta_{\text{MFBS}}(\delta = 16, \Delta t_s = 0.08$ s) $-\theta_{\text{FB}}(\delta = 1, \Delta t_s = 0.01$ s) is from -0.12 to 0.08 K, (Fig. 4c). Fig. 5b–d of

Part I show the differences between the MFB ($\delta = 16$, $\Delta t_s = 0.04$ s) and FB, which range from -0.12 K to 0.1 K; between the HE-VI ($\Delta t_s = 0.02$ s) and FB they are from -0.02 to 0.03 K. The accuracies are comparable between the MFBS with $\delta = 4$, $\Delta t_s = 0.04$ s and HE-VI with $\Delta t_s = 0.02$ s, as well as between the MFB with $\delta = 16$, $\Delta t_s = 0.04$ s and MFBS with $\delta = 16$, $\Delta t_s = 0.08$ s. However, the Δt_s for the MFBS is twice that for the MFB with the same δ . It is also noted that the HE-VI model becomes unstable when $\Delta t_s = 0.04$ s.

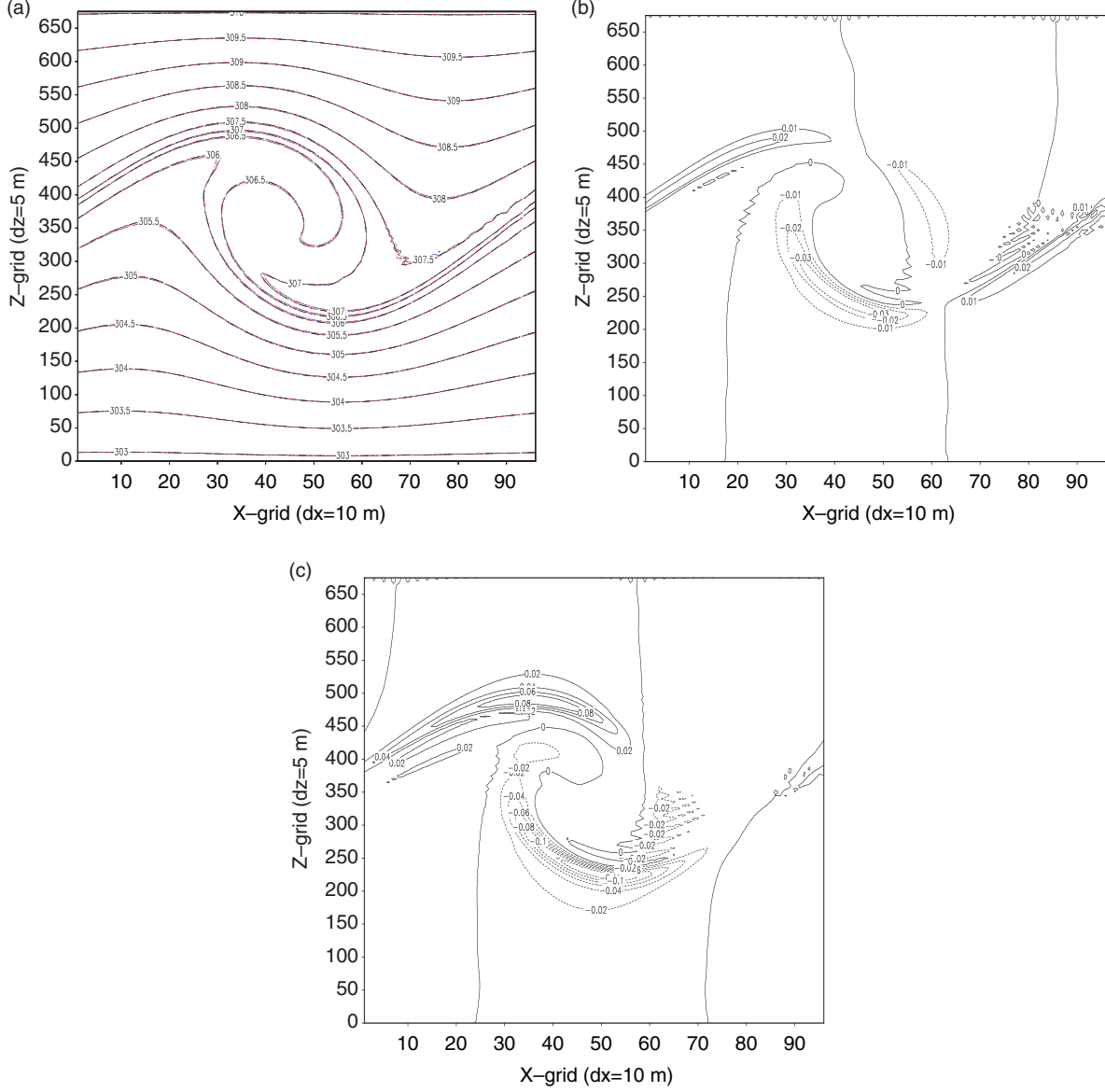


Fig. 4. Simulations for large-scale Kelvin-Helmholtz instability at $t = 320$ s with $\Delta t_b = 0.4$ s from (a) $\theta_{\text{FB}}(\delta = 1, \Delta t_s = 0.01$ s); MFB ($\delta = 16, \Delta t_s = 0.04$ s); MFBS($\delta = 4, \Delta t_s = 0.04$ s); MFBS ($\delta = 16, \Delta t_s = 0.08$ s), and HE-VI ($\Delta t_s = 0.02$ s); (b) $\theta_{\text{MFBS}}(\delta = 4, \Delta t_s = 0.04$ s) $-\theta_{\text{FB}}(\Delta t_s = 0.01$ s), contours from -0.03 to 0.03 K with interval of 0.01 K; (c) $\theta_{\text{MFBS}}(\delta = 16, \Delta t_s = 0.08$ s) $-\theta_{\text{FB}}(\Delta t_s = 0.01$ s), contours from -0.12 to 0.08 K with interval of 0.02 K.

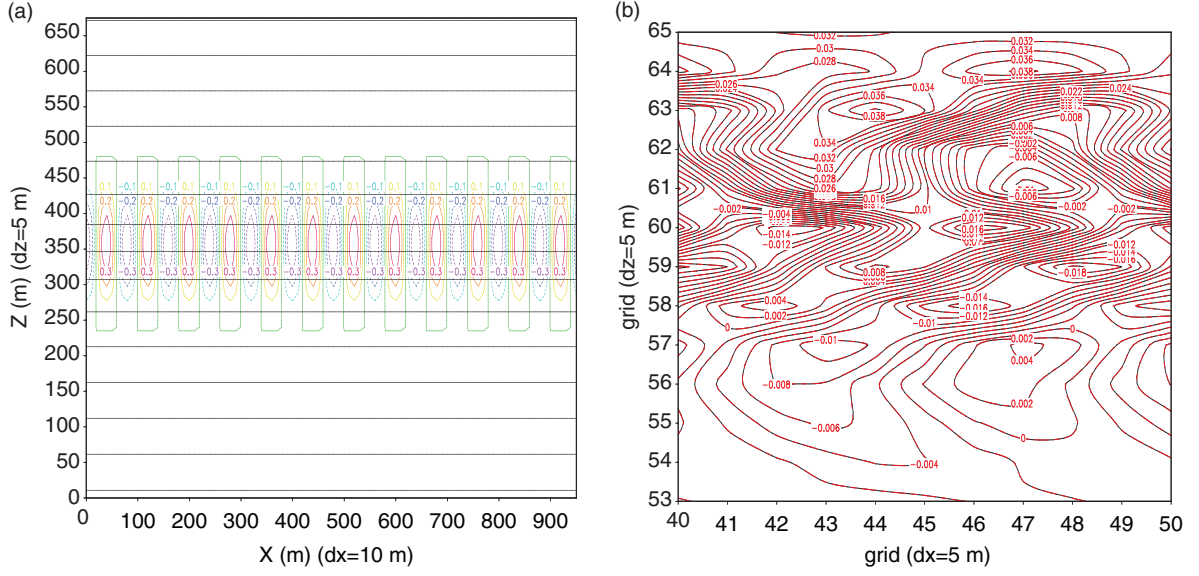


Fig. 5. As above but for small-scale Kelvin-Helmholtz instability simulation (a) initial background θ_0 (solid) and perturbation θ' (dash); (b) simulated θ' at $t = 240$ s from FB ($\delta = 1$, $\Delta t_s = 0.005$ s, red solid), and MFBS ($\delta = 16$, $\Delta t_s = 0.04$ s, blue dash). Contour interval is 0.002 K.

4.2. Small Kelvin-Helmholtz waves with $\Delta x = 5$ m, $\Delta z = 5$ m

The initial x-component wind and the background potential temperature are the same as in Section 4.1. The amplitude of initial potential temperature perturbation θ' is -0.4 K, which consists of sine-waves in the horizontal

with a wavelength of 40 m and an elliptic-type perturbation in the vertical with a radius of 120 m, as shown in Fig. 5a. Figure 5b shows the simulated θ' at $t = 240$ s with $\Delta t_b = 0.12$ s from FB with $\delta = 1$ and $\Delta t_s = 0.005$ s (solid line) and from MFBS with $\delta = 16$ and $\Delta t_s = 0.04$ s (dashed line). The temperature contours are virtually indistinguishable. The same holds for the velocity fields (not shown).

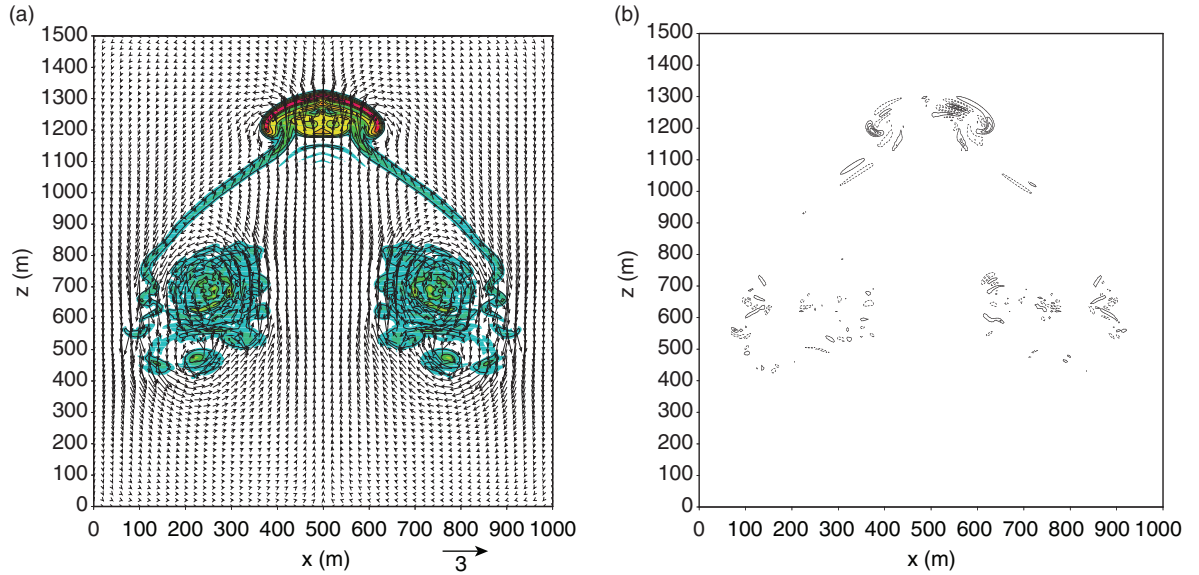


Fig. 6. Simulations at $t = 18$ min: (a) velocity V_{MFBS} and θ_{MFBS} ($\delta = 16$, $\Delta t_s = 0.06$ s, black contours), and θ_{FB} ($\Delta t_s = 0.008$ s, colour shaded), contours from -0.15 to 0.6 K; and (b) θ_{MFBS} ($\delta = 16$, $\Delta t_s = 0.06$ s) $- \theta_{FB}$ ($\Delta t_s = 0.008$ s), contours from -0.03 to 0.04 K.

However, the simulated temperature and velocity from HE-VI ($\Delta t_s = 0.005$ s) depart significantly from the FB with the same time interval, as discussed in Part I.

4.3. Thermal bubble without mean wind

The initial potential temperature of a thermal bubble with a Gaussian profile is shown in Fig. 8a of Part I, following eqs. (38) and (39) of Robert (1993). Simulations were performed with the same $\Delta x = \Delta z = 5$ m and $\Delta t_b = 0.12$ s as in Part I. The simulated θ and velocity vector at $t = 6$,

and 12 min of MFBS ($\delta = 16$ and $\Delta t_s = 0.06$ s) are almost identical to those of FB ($\delta = 1$ and $\Delta t_s = 0.008$ s) shown in Fig. 8b and c in Part I. Figure 6a shows the simulated θ_{MFBS} ($\Delta t_s = 0.06$ s with black contours) and θ_{FB} ($\Delta t_s = 0.008$ s with colour shaded plot) at $t = 18$ min for comparison. The difference between θ_{MFBS} and θ_{FB} ranges from -0.03 to 0.04 (Fig. 6b). Between θ_{MFB} ($\delta = 16$, $\Delta t_s = 0.03$ s) and θ_{FB} the difference ranges from -0.03 to 0.06 K, and for $\theta_{\text{HE-VI}}$ ($\Delta t_s = 0.008$ s) and θ_{FB} , from -0.3 to 0.2 K, as shown in Fig. 9c and d in Part I. The time interval Δt_s for the MFBS is twice that for MFB and almost eight times

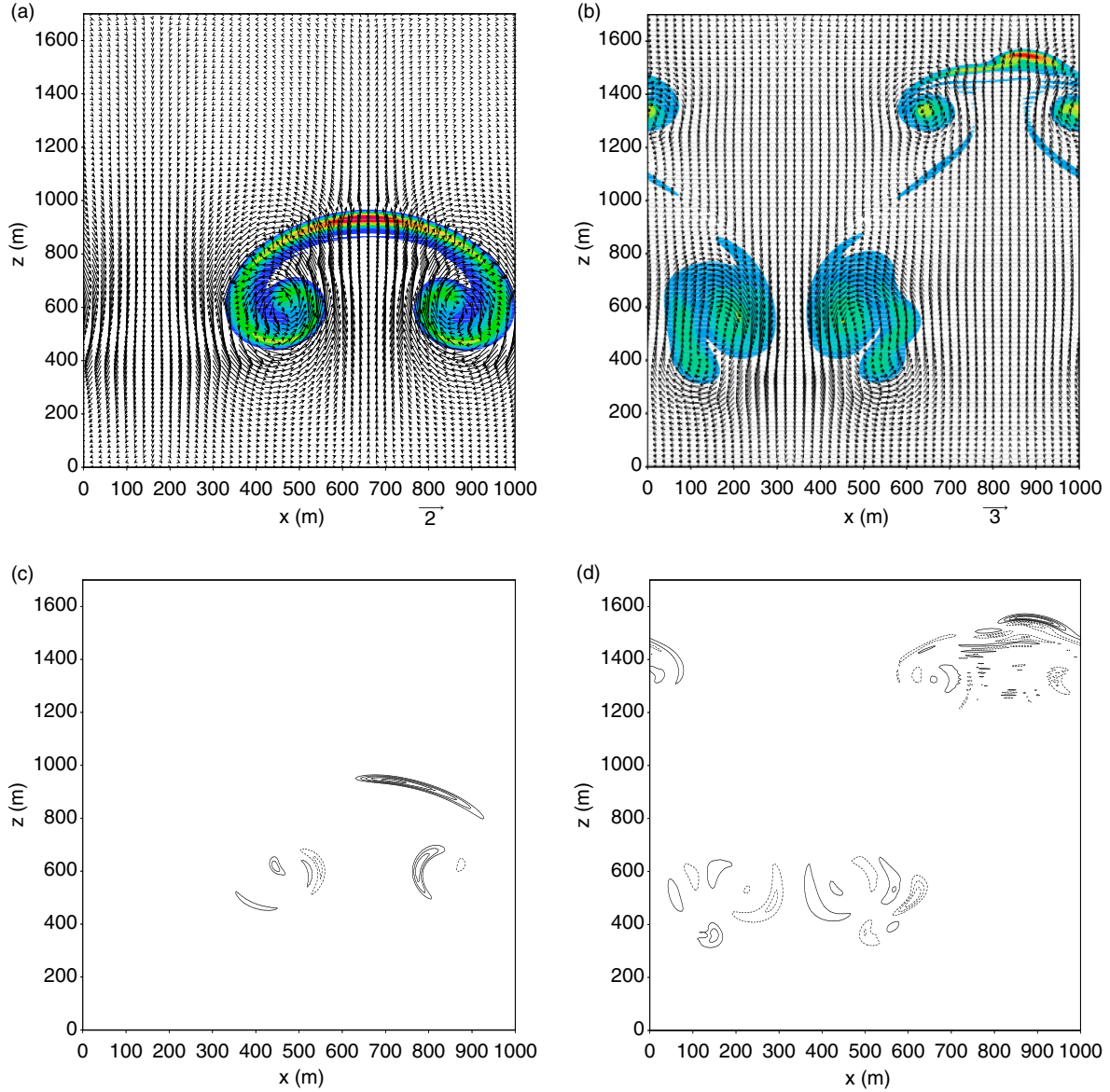


Fig. 7. (a) Simulated velocity perturbation V'_{MFBS} and θ_{MFBS} ($\delta = 16$, $\Delta t_s = 0.06$ s) at $t = 12$ min, (b) same as (a) but at $t = 24$ min, (c) $\theta_{\text{MFBS}} - \theta_{\text{FB}}$ ($\Delta t_s = 0.008$ s) at $t = 12$ min, contours from -0.004 to 0.006 with interval of 0.001 , and (d) $\theta_{\text{MFBS}} - \theta_{\text{FB}}$ at $t = 24$, contours from -0.015 to 0.02 K with interval of 0.005 K.

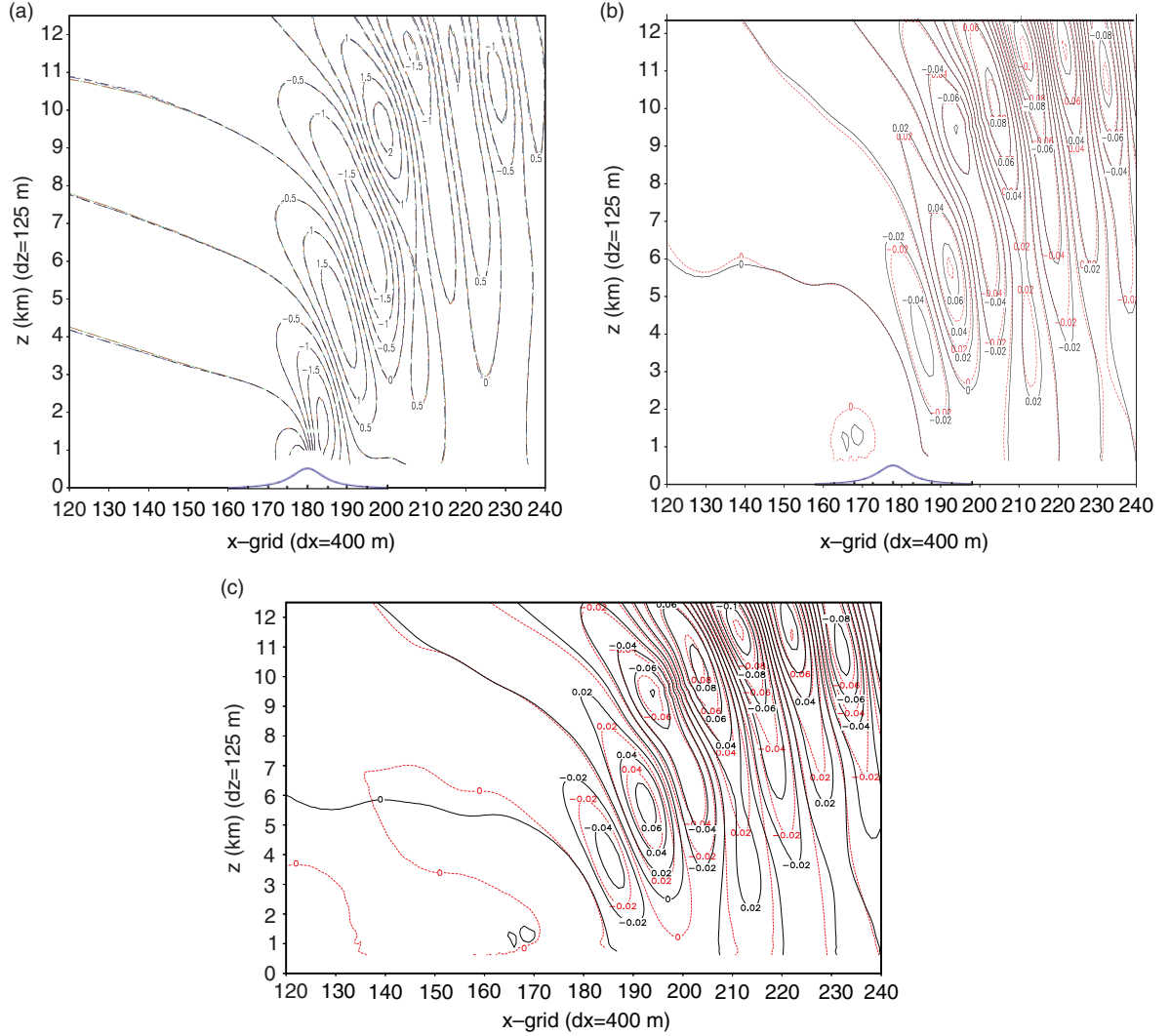


Fig. 8. Simulations at $t = 9000$ s with $\Delta x = 400$ m, $\Delta z = 125$ m and $\Delta t b = 10$ s: (a) $w_{\delta=1}$ ($\Delta t s = 0.25$ s, black dotted); $w_{\delta=16}$ ($\Delta t s = 1.0$ s, red short-dash); w_{MFBS} ($\Delta t s = 2.0$ s, $\delta = 16$, green long-dash); and $w_{\text{HE-VI}}$ ($\Delta t s = 1.0$ s, blue long-dash, short dash); (b) $w_{\delta=16} - w_{\delta=1}$ (red dash) and $w_{\text{MFBS}} - w_{\delta=1}$ (black solid); and (c) $w_{\text{HE-VI}} - w_{\delta=1}$ (red dash) and $w_{\text{MFBS}} (\delta = 16, \Delta t s = 2.0 \text{ s}) - w_{\delta=1}$ (black solid), the contour interval is 0.02 m s^{-1} .

that for HE-VI. Yet, the simulations using MFBS are as accurate as MFB and better than HE-VI. The simulations are also comparable to those of Robert (1993), Hsu and Sun (2001) and Chen and Sun (2001), etc., although the details depend upon the particular numerical schemes and turbulence parameterisations chosen for each model.

4.4. Thermal bubble with 10 m s^{-1} mean wind

The initial conditions are identical to those described in Section 4.3, except for the addition of a 10 m s^{-1} prevailing mean wind. This allows for an interaction between thermal convection and the mean wind, which is a more realistic

scenario than the previous case. The simulated potential temperature perturbation and velocity perturbation V' from the mean wind for the MFBS ($\delta = 16$ and $\Delta t s = 0.06$ s) 0.06 s) at $t = 12$ and 24 minutes are shown in Fig. 7a and b with a periodic boundary condition. The pattern is almost symmetric at $t = 12$ min and becomes more asymmetric with increasing time, because the x-component wind is slightly stronger on the windward side of the thermal. Figure 7b shows that the warm area shifts to the right-hand side of the front at $t = 24$ minutes. Differences from the FB ($\Delta t s = 0.008$ s) simulations remain small: between -0.004 and 0.006 K at $t = 12$ minutes, and between -0.15 and 0.2 K at $t = 24$ minutes (Fig. 7c and d).

4.5. Mountain waves

A uniform 10 m s^{-1} wind flows over a bell-shaped mountain with a peak height of 500 m and a half-width of 2000 m. The background buoyancy frequency is 0.01 s^{-1} . The simulated w with $\Delta x = 400 \text{ m}$, $\Delta z = 125 \text{ m}$ and $\Delta t b = 10 \text{ s}$, at $t = 9000 \text{ s}$ from: FB with $\delta = 1$, $\Delta t s = 0.25 \text{ s}$; MFB with $\delta = 16$, $\Delta t s = 1.0 \text{ s}$; MFBS with smoothing, $\delta = 16$, $\Delta t s = 2.0 \text{ s}$; and HE-VI with $\Delta t s = 1.0 \text{ s}$ are shown in Fig. 8a. They coincide among each other. Figure 8b shows that the difference in simulated w between the FB ($\Delta t s = 0.25 \text{ s}$) and MFBS ($\delta = 16$, $\Delta t s = 2.0 \text{ s}$) at $t = 9000 \text{ s}$ ranges from -0.1 to 0.08 m s^{-1} (solid lines), and the difference between the FB and MFB ($\delta = 16$, $\Delta t s = 1.0 \text{ s}$) is also between -0.1 and 0.08 m s^{-1} (dashed lines). Similarly, the difference between the FB and HE-VI ($\Delta t s = 1.0 \text{ s}$) is between -0.1 m s^{-1} and 0.08 m s^{-1} (dashed line) in Fig. 8c. Hence, the accuracy is comparable among the MFB ($\delta = 16$, $\Delta t s = 1.0 \text{ s}$), MFBS ($\delta = 16$, $\Delta t s = 2.0 \text{ s}$ with smoothing) and HE-VI ($\Delta t s = 1.0 \text{ s}$).

5. Summary

In Part I, it was demonstrated that the MNH with a parameter δ (between 4 and 16) applied to the continuity equation can suppress high-frequency acoustic waves effectively without a significant impact on gravity waves, enabling the use of a longer time step. Here, we have added a smoothing to the right-hand side of the continuity equation in the MNH, allowing us to double once more the time interval which was used for the MFB in Part I. Both eigenvalue analyses and non-linear model simulations show that the smoothing does not significantly degrade the accuracy of the results. The MNHS approach is simple and can be easily incorporated into many different numerical schemes. Furthermore, the results do not depart from the conventional FB result, even when the time interval used for the MNHS is eight times that for FB. However, HE-VI simulations can be significantly different from FB even when using an identical time interval that is allowed by the CFL criterion, as discussed in Part I. When the aspect ratio is around 6, the same $\Delta t s$ can be applied to the MFBS and HE-VI, but the HE-VI still needs more computing time to solve a tri-diagonal matrix. Besides, the HE-VI results may depart from that of FB, as discussed in Part I. We conclude that the MNHS is more accurate and efficient than the HE-VI when the aspect ratio is small, as in the cases presented here.

6. Acknowledgements

We would like to thank Profs. Uyeda and Ohigashi, Kato San and Tsujino San at Nagoya University for their help

when the senior author was a Visiting Professor at the Hydrospheric Atmospheric Research Center (HyARC), Nagoya University. We also like to thank Mr. Seaman at Purdue Information Technology Center for his assistance during this study. The reviewers' comments are greatly appreciated. The computing facilities provided by Nagoya University, Purdue University and Taiwan High Performance Computing Center are highly appreciated as well.

References

- Chen, S. H. and Sun, W. Y. 2001. The applications of the multigrid method and a flexible hybrid coordinate in a nonhydrostatic model. *Mon. Weather Rev.* **129**, 2660–2676.
- Hsu, W.-R. and Sun, W. Y. 2001. A time-split, forward-backward numerical model for solving a nonhydrostatic and compressible system of equations. *Tellus*. **53A**, 279–299.
- Klemp, J. B. and Wilhelmson, R. B. 1978. The simulation of three-dimensional convective storm dynamics. *J. Atmos. Sci.* **35**, 1070–1096.
- Mesinger, F. and Arakawa, A. 1976. *Numerical Methods used in Atmospheric Models*. GARP Publication Series No. 14, WMO/ICSU Joint Organizing Committee, Paris, France, 64 pp.
- Robert, A. 1993. Bubble convection experiment with a semi-implicit formation of the Euler equations. *J. Atmos. Sci.* **50**, 1865–1973.
- Saito, K. 2007. Nonhydrostatic atmospheric models and operational development at JMA. *J. Meteor. Soc. Japan*. **85B**, 271–304.
- Sun, W. Y. 1980. A forward-backward time integration scheme to treat internal gravity waves. *Mon. Weather Rev.* **108**, 402–407.
- Sun, W. Y. 1984. Numerical analysis for hydrostatic and non-hydrostatic equations of inertial-internal gravity waves. *Mon. Weather Rev.* **112**, 259–268.
- Sun, W. Y. 2011. Instability in leapfrog and forward-backward schemes: part II: numerical simulation of dam break. *J. Comput. Fluids*. **45**, 70–76.
- Sun, W. Y. and Sun, O. M. T. 2011. A modified leapfrog scheme for shallow water equations. *J. Comput. Fluids*. **52**, 69–72.
- Sun, W. Y., Sun, O. M. T. and Tsuboki, K. 2012. A modified atmospheric nonhydrostatic model on low aspect ratio grids. *Tellus A*. **64**, 17516.
- Tsuboki, K. and Sakakibara, A. 2002. Large-scale parallel computing of Cloud Resolving Storm Simulator. In: *High Performance Computing* (eds. H. P. Zima, K. Joe, M. Sato, Y. Seo, and M. Shimasaki) Springer Verlag, Berlin, Germany, pp. 243–259.
- Tsuboki, K. and Sakakibara, A. 2007. Numerical prediction of high-impact weather systems. 2-15 December 2007. In: *The Seventeenth IHP Training Course (International Hydrological Program)*, Nagoya University and UNESCO, Nagoya, Japan, 273 pp.